Experimental and Theoretical Studies of the Multistability in the Electroreduction of the Nickel(II)−N_3^- Complexes at a Streaming Mercury Electrode

Rafał Jurczakowski and Marek Orlik*

Laboratory of Electroanalytical Chemistry, Department of Chemistry, University of Warsaw, ul. Pasteura 1, PL-02-093 Warsaw, Poland

Received: April 9, 2003; In Final Form: July 9, 2003

Following our earlier experimental and theoretical studies of the self-organization in the Ni(II)−SCN^- electroreduction at the streaming mercury electrode we describe analogous phenomena for the *azide* complexes of nickel(II). The complex electrochemical mechanism of this process is a source of *multistability*, if the appropriate serial ohmic resistance is present in the electric circuit. In dependence of the solution composition, *bistability* and *tristability* in the response of the electric current vs the applied voltage was observed. No spontaneous oscillations were reported for the studied process. The $I-E$ characteristics of the Ni(II)−N_3^- electroreduction, which exhibits the region of the negative differential resistance (NDR), are the source for the bistable behavior. If the composition of the sample is adjusted so that the current of the Ni(II) electroreduction in the NDR region overlaps significantly with the extra current, originating presumably from the catalytic reduction of azide ions, the second NDR region is also formed, and these complex characteristics are a source of the tristable behavior. The theoretical description of the observed multistable phenomena was made in terms of both the theory of electrode processes at a streaming electrode and standard techniques of nonlinear dynamics. The linear stability analysis led to theoretical bifurcation diagrams similar to the experimental ones. The reported tristability seems to be one of the first experimental examples of such a behavior in electrochemical systems and one of only a few of its manifestations in chemical systems in general.

1. Introduction

The dynamic behavior of the far-from-equilibrium physicochemical systems may exhibit various types of spontaneous self-organization as a function of the temporal and/or spatial coordinates.[1−9] The examples of such phenomena include synchronic oscillatory changes of the whole system's state or the local onset of spatiotemporal patterns progressing through the reaction medium. Beyond the oscillatory regime, the characteristics of the nonequilibrium steady states may correspond either to a trivial case of monostability or to the *multistability*, i.e., to the coexistence of more than one stable steady state for the same set of control conditions. Also more complex phenomena were reported in the literature, e.g. bistability involving coexistence of a steady state and sustained (stable) oscillations,[10] or birythmicity, when two different oscillating regimes can be attained from different initial states for the same final set of control parameters.[11] Studies of such dynamical phenomena remain one of the modern scientific disciplines, due to the pioneer works by Prigogine et al. (cf., e.g., refs 1 and 2), the recent development of the modern computational techniques and increasing number of the experimental observations of such phenomena in various systems.[3−9] In conjunction with that, it is noteworthy that the principal formal mathematical characteristics of self-organization phenomena exhibit distinct similarities, which emphasizes universalities in such dynamical behaviors.

This paper is devoted to the phenomenon of multistability. In the multistable regime, the actually observed state depends on the past history of the system, which in this way exhibits the so-called "memory effect". A review of literature data shows that in experimental practice the manifestation of multistability in most cases is limited to a bistable behavior, which was found for quite many homogeneous and heterogeneous systems (cf., e.g., refs 2, 5, 7, and 9). Examples of tristability were rather rarely reported for real chemical processes. In *homogeneous* systems, such a behavior can be unequivocally diagnosed only in flow (CSTR) reactors. Orbán et al.[10] described tristability for the complex (chemically coupled) $ClO_2^--I^--IO_3^--H_3AsO_3$ oscillator. Nagy and Treindl[12] observed it for the $MnO_4^--H_2O_2-H_3PO_4$ system, belonging to the class of the so-called permanganate oscillators. Recently Chie et al.[13] reported tristability for the $BrO_3^--SO_3^{2-}-HCO_3^-$ pH-oscillator. The potential existence of tristability was also analyzed theoretically for conditions of the CSTR reactors: Tockstein[14] described simple kinetic models with autocatalytic steps that theoretically could produce tristability whereas Ganapathisubramanian[15] postulated the existence of tristability for the $IO_3^--H_3AsO_3$ system in a conventional CSTR system, complicated with the attached satellite reactor. For *heterogeneous* electrochemical systems, apparently the first examples of the tristable behavior were described only in 1998−2000 by Schell and Chen[16−18] for the *galvanostatic* oxidations of primary alcohols (methanol, ethanol, 1-butanol) at a rotating disk Pt electrode. The observed tristability involved either three coexisting steady states (as in homogeneous systems) or a single oscillatory state coexisting with two steady states.

Our experimental system exhibiting both bistability and tristability is different, since (i) it is based on the electroreduction of the azide complexes of Ni(II) at mercury, for which process,

* To whom correspondence should be addressed. E-mail: morlik@chem.uw.edu.pl. Fax: +48 22 822 59 96. Telephone + 48 22 822 02 11 ext. 245.

10.1021/jp0349482 CCC: $25.00
Published on Web 08/22/2003

to our knowledge, only classical electrode kinetics were analyzed so far,[19] and (ii) it involves the control of the external voltage whereas the electric current is an observed system response. In view of the rather limited number of known examples of tristability, the description of such a new type of the tristable system is advantageous also for the illustration of one more possible mechanism underlying this type of behavior.

In this paper, we present the representative experimental results for the studied process and analyze them theoretically in terms of the following: (i) the theory of the faradaic and capacitive currents at the streaming electrodes and (ii) a linear stability analysis leading to the bifurcation diagrams.

2. Experimental Section

The *experimental* methodology was principally the same as in our previous works,[20,21] in which we described the special construction and application of the *streaming mercury electrode* to the studies of the sustained oscillations and bistability in the electroreduction of thiocyanate complexes of Ni(II).

The solutions of azide complexes of nickel(II) were prepared ex tempore by mixing of appropriate amounts of aqueous solutions of nickel(II) perchlorate with the solution of sodium azide. Crystalline nickel(II) perchlorate, $Ni(ClO_4)_2 \cdot 6H_2O$ was obtained by neutralization of the p.a. basic nickel(II) carbonate (POCh) with the appropriate amount of p.a. perchloric acid (APOLDA), followed by recrystallization from water. The concentration of Ni^{2+} in the stock solutions of this salt was determined by complexometric titration with EDTA.[22] Commercially available p.a. NaN_3 (Fluka) was used without further purification. For varying NaN_3 concentrations the constant ionic strength of the solutions was maintained by addition of appropriate amounts of p.a. $NaClO_4$ (APOLDA), purified by prior recrystallization from water. For all solutions the triply distilled water, additionally purified in a final step using Millipore filters, was used.

Prior to measurements the sample solutions were thoroughly deaerated using pure argon (5.0, Praxair). It had been additionally purified from traces of oxygen by passage through a glass column filled with heated copper wires, obtained from the p.a. cupric oxide ($CuO + Cu_2O$) wires (POCh), which had been reduced to the metal by gaseous hydrogen at the appropriately enhanced temperature.

As the working electrode the streaming Hg electrode, filled with p.a. mercury (POCh) was used. The construction of this electrode was described in detail in our previous paper.[20] Using this streaming electrode, the voltammetric characteristics of the process studied were recorded with the EG&G/PARC potentiostat model 263A and model 273, controlled by IBM PC compatible computer with the commercial software: PowerStep version 1.12.00 (for model 263A) and Headstart version 1.4 (for model 273). The Headstart source code was adapted to our requirements with kind permission of the EG&G Co.

Double layer capacitances were determined using the dropping mercury electrode with an ac OH-105 polarograph (Radelkis), for ac amplitude 5 mV and frequency 60 Hz. The ac currents, recorded for samples studied, were recalculated into capacitances by comparison with ac currents corresponding to 0.10 mol dm^{-3} KCl solution of known capacitances.[23]

In all measurements the three-electrode potentiostatic circuit was applied. The serial ohmic resistance R_s, which for the studies of multistability was switched between the streaming Hg electrode and the slot of the working electrode of the potentiostat, was supported by the decade resistor RU-71 (Urania), with the maximum resolution of 0.1 Ω. The total voltage applied between the working and the reference electrodes will be further denoted by U, whereas the interfacial potential drop, smaller than U for the magnitude of ohmic drops IR_s, will be denoted by E. The saturated (KCl) calomel reference electrode (SCE) was separated from the studied solution with a salt bridge and the uncompensated ohmic drops were minimized by using the Luggin capillary. The platinum wire ($A \approx 2$ cm^2) served as a counter electrode.

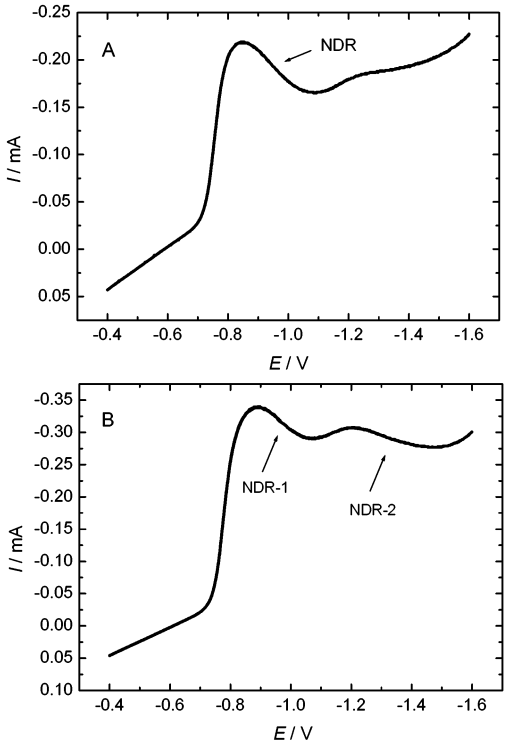

Figure 1. Current-potential ($I-E$) dependencies for the samples: (A) 2.0 mmol dm^{-3} $Ni(ClO_4)_2$ + 1.0 mol dm^{-3} NaN_3 + 6 mmol dm^{-3} $HClO_4$ and (B) 4.0 mmol dm^{-3} $Ni(ClO_4)_2$ + 2.0 mol dm^{-3} NaN_3 + 12 mmol dm^{-3} $HClO_4$, recorded at the streaming mercury electrode for zero serial resistance ($R_s = 0$) in the circuit of the working electrode. The regions of the negative differential resistance (NDR, $dE/dI < 0$) starting from ca. −0.85 V, are distorted by the extra faradaic current which in part B leads to the formation of two (NDR-1, NDR-2) sequential regions of negative resistance. Parameters of the streaming electrode: capillary flow $m = 212$ mg s^{-1}, internal glass capillary (=cylindrical mercury electrode) diameter $\phi = 0.11$ mm, length of mercury jet (directed upward) $l_{max} = 2.85$ mm.

All measurements were done for the temperature 298.15 ± 0.10 K, controlled by the ultrathermostat U4 (VEB MLW Prüfgeräte-Werk Medingen, Dresden, Germany).

Numerical calculations were done in Pascal with an IBM PC Pentium III machine.

3. Results

3.1. The Negative Differential Resistance (NDR) in the Ni(II)—N_3^- Electroreduction. Figure 1 shows two representative voltammetric $I-E$ curves of the Ni−N_3^- electroreduction at the streaming Hg electrode for the samples of different concentrations of NaN_3 and added small amounts of perchloric acid. With respect to the latter reagent, one should note that any sample prepared by direct mixing of pure solutions of $Ni(ClO_4)_2$ and excess NaN_3 yielded always drawn-out and rather irreproducible curves, presumably due to the formation and even precipitation of the hydroxyl species of Ni(II) ions, appearing in slightly basic medium of hydrolyzing azide ions ($pK_a = 4.44$ at ionic strength = 1.0; see ref 24). Therefore, to obtain smooth,

reproducible $I-E$ response, every sample had to be slightly acidified with $HClO_4$ (we chose 6 mmol of perchloric acid for every 1 mol of azide anions). The pH of samples prepared in this way was equal to ca. 6.3 ± 0.1.

Figure 1 shows that the $I-E$ dependencies for the $Ni^{2+}-N_3^-$ electroreduction are more complex that those for the $Ni^{2+}-SCN^-$ electroreduction under comparable conditions,[20] since in the present case the region of a negative differential resistance (NDR) is distorted by the relatively small contribution from the extra faradaic current. For the conditions from Figure 1B, this distortion is so substantial that it appears sufficient to produce even *two* sequential regions of NDR. Such a complex $I-E$ characteristics of the electrochemical cell should obviously lead to appropriately complex types of the dynamic behavior, if the serial ohmic resistance which meets the instability conditions[21] is switched into the circuit. For the case considered here, it appears that for certain ranges of the applied external voltage U and of the serial resistance R_s the loss of the stability of a single steady state turns into the coexistence of more than one steady state, i.e., multistability. These phenomena are described below in more detail.

3.2. Bistability in the Ni(II)—N_3^- Electroreduction. First we describe the nonequilibrium phenomena that are associated with the $I-E$ characteristics of the Ni(II)−azide electroreduction from Figure 1A. The appropriately high serial ohmic resistance, switched into the circuit with such characteristics causes the *bistable* behavior of the studied process which is detected as the *hysteresis* in the current response as a function of the cyclic changes of the external voltage U. Within the bistable region of $U \in [U_{c,1}; U_{c,2}]$ the system's state is thus dependent upon its history ("memory effect"). The exemplary experimental manifestations of this bistability, for two different serial resistances R_s, are shown in Figures 2A and 3A.

Figures 2A and 3A show only *stable* steady states since only such ones can be observed experimentally. The directly unobservable *unstable* steady states of this system, located between the stable ones and composing with them a characteristic folded shape of all steady states, can however be easily found, as we showed in our previous paper,[20] by translation of the $I-E$ characteristics from Figure 1A, point by point, along the U axis, for the values of ohmic drops IR_s corresponding to actual resistance: $R_s = 7$ or 13 kΩ, in dependence of the experimental conditions from Figures 2A or 3A, respectively. The full folded diagrams of stable and unstable steady states, obtained in this way are shown in Figures 2B and 3B. Slight discrepancies, observed particularly at the edges of these folded shapes, compared to the experimental diagrams of stable steady states, are most probably caused by the imperfect characteristics of the real streaming electrode, involved in the intense hydrodynamic flow of the solution dragged by the mercury stream.[25,26] Also, some elements of the electric circuit may contribute to the overall resistance that therefore may be slightly higher than the R_s value. A more strict mathematical way of reconstructing the full shape of the folded diagram of the stable and unstable steady states will be given in the Discussion.

Systematic studies of the dynamic regimes of the system with the $I-E$ characteristics from Figure 1A, observed for certain range of the external voltage U and of the serial resistance R_s, allowed us to construct the experimental stability (bifurcation) diagram which is shown in Figure 4. It is noteworthy, that contrary to the analogous diagram for the Ni(II)−SCN^- electroreduction,[20] the region of the spontaneous, sustained oscillations was actually *not* detected within the studied parameters range.

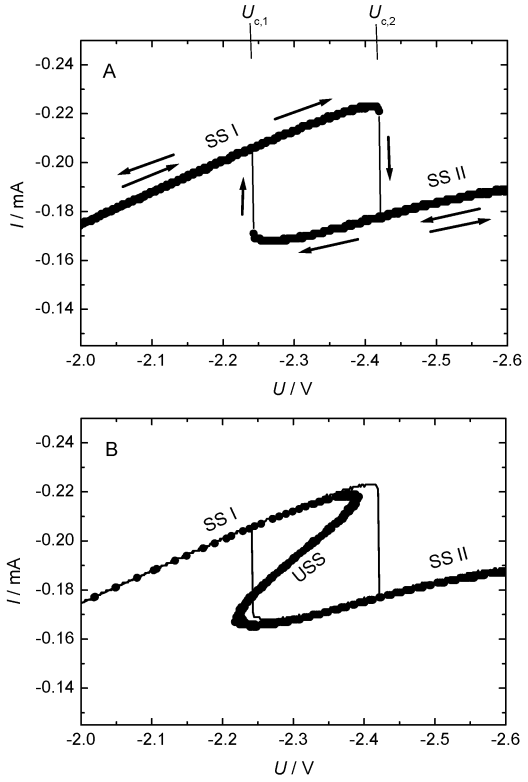

Figure 2. (A) Bistable behavior in the electroreduction of the azide complexes of nickel(II) at a streaming mercury electrode, manifesting itself as the hysteresis in attaining the sets of "high-current" (SS I) or "low-current" (SS II) steady states as a function of the direction of the linear voltage (U) scan. Within the interval $[U_{c,1}, U_{c,2}]$ the system is bistable, whereas outside this region remains monostable. The composition of the sample and the parameters of the streaming electrode are the same as for Figure 1A, except for the serial resistance $R_s = 7$ kΩ; (B) the corresponding full diagram of stable (SS I, SS II) and unstable (USS) steady states obtained by translation, along the voltage axis, of the $I-E$ curve from Figure 1A for the actual ohmic drops IR_s (see text for detailed explanation).

3.3. Tristability in the Ni(II)—N_3^- Electroreduction. When the appropriate serial ohmic resistance was switched into the circuit of the system of the $I-E$ characteristics from Figure 1B, i.e., with a sequence of *two* regions of negative differential resistance, not only the bistable but also the *tristable* behavior was detected during the cycling scan of the external voltage U. The three stable steady states: the "high-current", SS I, the "low-current", SS II, and the additional "middle-current", SS III, are then observed experimentally for the same range of control parameters (U, R_s). The illustration of such a behavior, for the exemplary ohmic resistance $R_s = 14$ kΩ, is shown in Figure 5A.

It is noteworthy that in order to cover the *full* region of existence of SS III states during the voltage scan from the negative toward positive values, it is necessary to realize the *local* voltage scan toward both less negative and more negative voltage limits of the SS III branch, after the current jump from SS II states (at ca. −5.33 V) to the middle of the SS III branch. This was done by the appropriate modification of the source code of the HEADSTRT program for the EG&G 273 potentiostat. To summarize, at ca. −5.1 V the transition of the monostable (SS I) to bistable (SS I + SS III) behavior occurs, which at ca. −5.3 V transforms into the tristable (SSI + SS II + SS III) regime, followed by the switch to the bistable (SS I + SS II) regime at ca. −5.52 V, and finally the system becomes again monostable, but now remaining in the stable steady-state SS II.

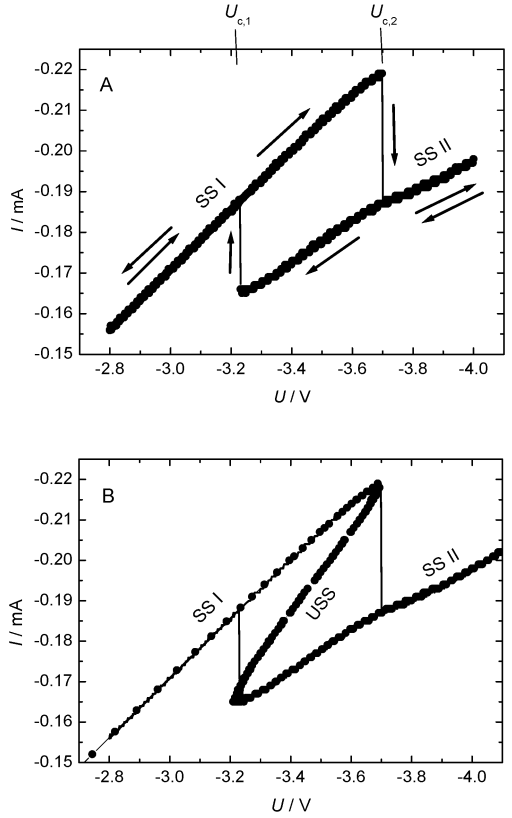

Figure 3. (A) Experimentally found bistability and (B) the corresponding full diagram of stable and unstable steady states for the Ni(II)−N_3^- electroreduction with the $I-E$ characteristics from Figure 1A and the ohmic resistance $R_s = 13$ kΩ. For further explanation, see text and caption to Figure 2.

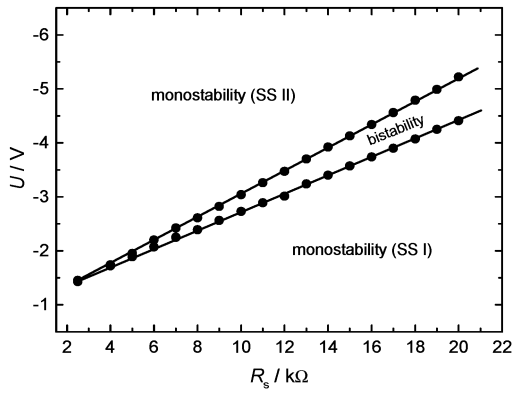

Figure 4. Stability (bifurcation) diagram of the dynamic nonequilibrium steady-state states observed for the electroreduction of azide complexes of nickel(II) at a streaming mercury electrode, with the current−voltage characteristics from Figure 1A. The lines, led through experimental points (●), determine the position of the saddle-node bifurcations, separating the regions of the monostable and the bistable behavior of the system.

Analogously to the full characteristics of the bistable regions from Figures 2 and 3, it is obvious that in the case of tristability between every pair of the neighboring *stable* steady states also the corresponding *unstable* steady states have to exist, the position of which completes the full, now double-folded diagram of all steady states. As before, one obtains this diagram from the direct experimental data, by translation of the $I-E$ curve from Figure 1B along the U axis, for the actual ohmic drops IR_s. Results of such a transformation are shown in Figure 5B.

Systematic studies of the transitions between the monostable and multistable behaviors for this system as a function of control

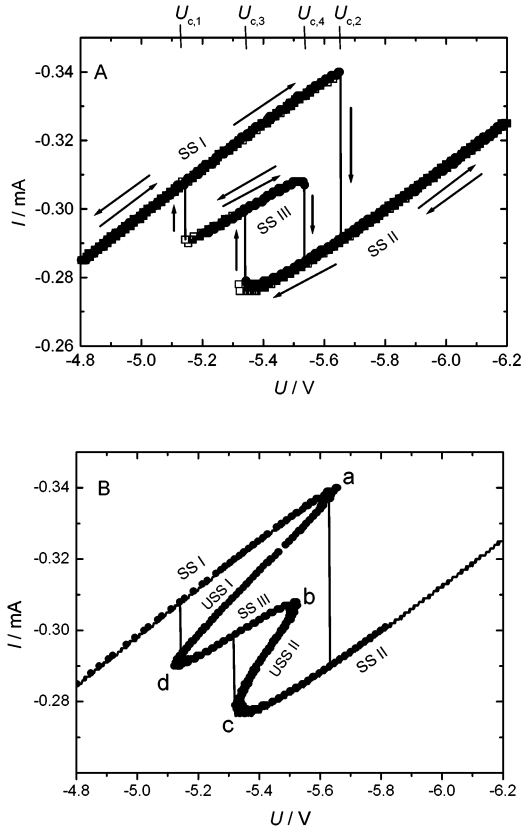

Figure 5. (A) Bistable and tristable behaviors for the electroreduction of the azide complexes of nickel(II) at a streaming mercury electrode. Tristability manifests itself as the complex scheme of hysteresis, indicating the coexistence of sets of SS I, SS II, and SS III stable steady states for the same control parameter (U), for the exemplary constant serial resistance $R_s = 14$ kΩ; (**B**) the corresponding full diagram of stable (SS I, SS II, SS III) and unstable (USS I, USS II) steady states obtained by translation, along the voltage axis, of the $I-E$ curve from Figure 1B for the actual ohmic drops IR_s; letters (a, b, c, d) denote the edges of the folds at which the monostable/bistable and bistable/tristable transitions occur, for comparison with the experimental stability (bifurcation) diagram in Figure 6.

parameters (U, R_s) allowed us to construct the experimental bifurcation diagram, shown in Figure 6. Also this diagram does not exhibit any region of oscillations.

One may add, that analogous transitions between the monostable, bistable, and tristable behaviors were observed also for other compositions of the samples, provided that their $I-E$ characteristics exhibited two sequential regions of the NDR (for example, see Figure 7).

4. Discussion

4.1. The Role of Azide Ions in the Shape of the $I-E$ Characteristics of the Electroreduction of Azide Complexes of Nickel(II). For the complete understanding of the reported multistable phenomena one has to establish first the composition of the reactant−azide complexes of nickel(II) forming in the studied solutions and recognize their electroreduction mechanism that explains the $I-E$ characteristics from Figure 1. A more detailed electrochemical analysis of this problem will be presented elsewhere,[27] whereas here only those characteristics of the studied process will be summarized which are crucial for the nonlinear dynamical phenomena discussed.

On the basis of literature studies,[19,28,29] one can conclude that, in our case, for samples with 2 mol dm^{-3} NaN_3, most of nickel(II) ions were present in the form of the anionic $[Ni(N_3)_4]^{2-}$

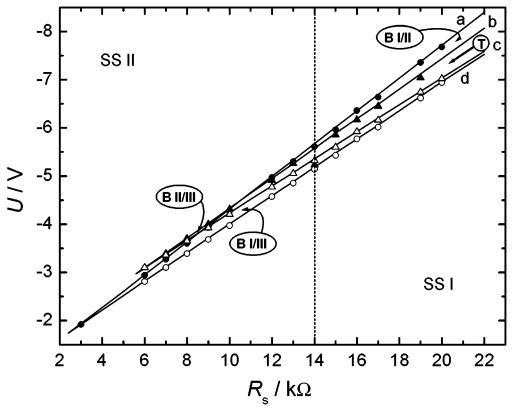

Figure 6. Experimental stability (bifurcation) diagram of the monostable, bistable (B I/II, B I/III, B II/III) and tristable (T) regions involving stable steady states SS I, SS II, SS III for the electroreduction of azide complexes of nickel(II) represented by $I-E$ characteristics from Figure 1B. The (a, b, c, d) letters at the corresponding lines refer to edges of folds in Figure 5B, the positions of which on the voltage axis determine the borderlines of the monostable/bistable and bistable/tristable transitions (saddle-node bifurcations). The vertical dotted line at $R_s = 14$ kΩ indicates such transitions as shown in Figure 5.

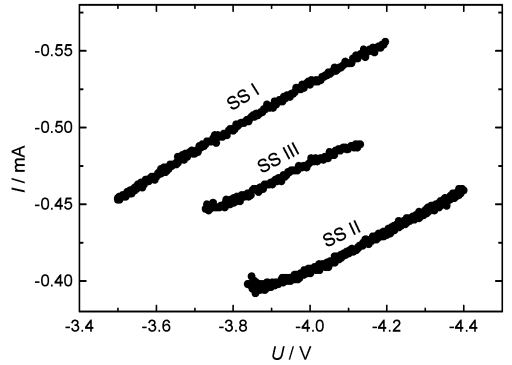

Figure 7. Monostable, bistable, and tristable regions of the dynamic behavior, involving SS I, SS II, and SS III stable steady states, detected for the electroreduction of 8 mmol dm^{-3} $Ni(ClO_4)_2$ + 2 mol dm^{-3} NaN_3 + 12 mmol dm^{-3} $HClO_4$, with the serial ohmic resistance in the circuit $R_s = 6$ kΩ.

complex whereas for 1 mol dm^{-3} NaN_3 some amounts of $Ni(N_3)_2$ and $Ni(N_3)^+$ also coexisted in equilibrium. On the basis of our analysis of the electrode process, we came to the following two main conclusions: (i) the mechanism of the formation of the NDR region for the electroreduction of azide complexes of nickel(II) is most probably analogous to that for the thiocyanate complexes of nickel(II)[30−34] and indium(III),[34−37] i.e., the rate of the electroreduction of azide complexes of nickel(II) decreases stepwise at potentials more negative than the potential of zero charge, due to progressing desorption, from the electrode surface, of the electrocatalytic azide ions from the mercury surface; (ii) the deformation of the $I-E$ curve, leading to the double NDR region, is caused by the extra faradaic process in the form of a small wave of a rather well-defined plateau which overlaps with the original NDR region. According to the results of our recent electrochemical studies,[27] it is probable that this small extra faradaic current, rising with H^+ concentration, originates from the electroreduction of azide ions (catalyzed by electroreduction of Ni(II) ions), with the formation of ammonia (or ammonium cations) as at least one of the products. More precisely, for the present analysis as the most probable reaction scheme, we assume the two-electron reduction of the azide anion, leading to ammonia and free nitrogen. Such a scheme explains why H^+ ions, originating from added $HClO_4$, are necessary for the flow of this extra faradaic current, since they are required for the formation of NH_3 as one of the thermodynamically stable products. It is useful to explain here that at this stage of our investigations for the control of pH of the samples, we did not use any special buffer but only small amounts of $HClO_4$, to avoid the eventual formation of mixed complexes of nickel(II) cations with azide anions and the components of the buffer. The formation of such species, of unknown stoichiometry, is quite probable because of a relatively low thermodynamic stability of Ni(II)−N_3^- complexes (β_1 = 7−11, cf. ref 19). The addition of small amounts of $HClO_4$ guaranteed that the azide complexes of nickel(II) remained the only electroactive reactants.

For the description of the magnitude of the faradaic currents, it is further noteworthy that even despite this extra small faradaic contribution, discussed above, the maximum currents of all $I-E$ characteristics, like those shown in Figure 1, remained always *below* the limiting, diffusion-controlled value, which can be calculated from the following equation:[38]

$$I_d = -\frac{4nFD_{ox}^{1/2}m^{1/2}l_{max}^{1/2}c_{ox}^0}{\rho_{Hg}^{1/2}} \quad (1)$$

with the diffusion coefficient of azide complexes of nickel(II): $D_{ox} = 6.9 \times 10^{-6}$ cm^2 s^{-1}.[19] This observation is understandable since the rate of electroreduction of azide complexes of nickel(II) is generally lower ($k_s^{app} \approx 5 \times 10^{-5}$ cm s^{-1}) than that of its thiocyanate complexes ($k_s^{app} \approx 0.001$ cm s^{-1}) for which a diffusion-controlled plateau was attained before the NDR region.[20] Of course, for lower apparent rate constant the limiting current of Ni(II)−N_3^- complexes theoretically could be obtained at more negative potentials, but in this case the progressing desorption of electrocatalytic azide ions limits the overall rate of the electrode process and prevents the faradaic current to reach its diffusion-controlled value within the entire potential range studied.

4.2. The Multistability in the Ni(II)−N_3^- Electroreduction in Terms of the Characteristics of the Electric Circuit. On the basis of the $I-E$ characteristics from Figure 1 treated analogously as the typical characteristics of the electronic circuit with the element of the N-shaped negative resistance, connected in series with ohmic resistance, one can easily—qualitatively and quantitatively—predict the existence of the bistable and tristable behavior in our system. The possible stable and unstable steady states correspond to the cross sections of the steady-state N-shaped $I-E$ characteristics of the electrochemical system with the load line $I = U/R_s - E/R_s$.[9,39] Figure 8 shows how the position of such load lines, plotted for the constant resistance R_s and varying external voltages U, together with the experimental $I-E$ characteristics from Figure 1B, determine the critical voltages for transitions between the bistable and tristable behaviors, in a good concordance with the experimental results (cf. Figure 5).

This is a simple illustration of the obvious conclusion that in the electrochemical systems of the type studied by us the coexistence of M stable steady states in the presence of nonzero serial resistance R_s requires the existence of a sequence of $M - 1$ regions of a negative polarization resistance in the $I-E$ characteristics for zero serial resistance.

4.3. Theoretical Electrochemical Description of the Multistability in the Ni(II)—N_3^- Electroreduction. The purpose of this section is to show the method of construction of the

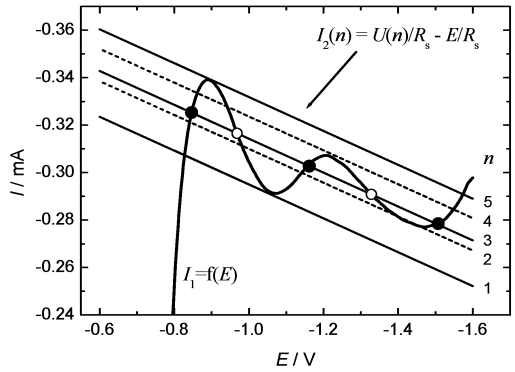

Figure 8. Intersections of the enlarged part of the experimental N-shaped characteristics from Figure 1B (denoted here as $I_1 = f(E)$) with the load line $I_2 = (U-E)/R_s$, explaining the occurrence of tristability and bistability, for the exemplary constant serial $R_s = 14$ kΩ and different externally applied voltages U: (1) −5.130, (2) −5.340, (3) −5.400, (4) −5.531, and (5) −5.646 V. As an example, for the load line (3) the associated stable (●) and unstable (○) steady states are indicated.

diagrams of multiple steady states in the Ni(II)−N_3^- electroreduction on the basis of its purely electrochemical characteristics. Such an approach needs the formulation of the model of this process and the determination of its thermodynamic and kinetic parameters.

4.3.1. The Model of the Ni(II)—N_3^- Electroreduction and Determination of Parameters. The kinetic and thermodynamic parameters of the electrode process were found from the comparison of the experimental $I-E$ characteristics from Figure 1, parts A and B, respectively, with the $I-E$ dependencies calculated theoretically for the following model scheme:

$$Ox_1 + n_1 e \underset{k_{b,1}}{\overset{k_{f,1}}{\rightleftharpoons}} Red_1 \quad (2)$$

$$Ox_2 + n_2 e \underset{k_{b,2}}{\overset{k_{f,2}}{\rightleftharpoons}} Red_2 \quad (3)$$

with $Ox_1 \equiv [Ni(N_3)_p]^{(2-p)+}$, $Red_1 \equiv Ni(Hg)$, $n_1 = n_2 = 2$, Ox_2 = reducible $\{N_3^-, H^+\}$ species, and $Red_2 = \{NH_3$ (or $NH_4^+) + N_2\}$. Despite the formal simplicity of this scheme, the complicated shape of the corresponding $I-E$ characteristics is hidden in the complex dependencies of its rate constants on the electrode potential. Thus, in eq 2, Ox_1 species undergoes parallel reduction according to (i) the catalytic (inner-sphere) pathway, with apparent, formally potential-dependent standard rate constant $k_{s,I}^{app}$, explaining the formation of the main electroreduction wave of Ni(II) with the single NDR region, and (ii) the noncatalytic (outer-sphere) pathway, with the apparent standard rate constant $k_{s,II}^{app}$, explaining the slight rise of the faradaic current at extremely highly negative potentials. In eq 3, the Ox_2 species is reduced with the apparent standard rate constant $k_{s,2}$, and in this way, it yields the small extra faradaic current distorting the NDR region. Accordingly, the following expressions were assumed for the dependence of the rate constants $k_{f,1}$, $k_{b,1}$, $k_{f,2}$, and $k_{b,2}$ on the electrode potential.

For the process in (2)

$$k_{f,1} = k_{s,I}^{app}\left\{\frac{1}{1+\exp[P_1(E-P_2)]}\right\}\exp[-(\alpha n)_I f(E-E_{f,1}^0)] + k_{s,II}^{app}\exp[-(\alpha n)_{II} f(E-E_{f,1}^0)] \quad (4)$$

$$k_{b,1} = k_{f,1}\exp[nf(E-E_{f,1}^0)] \quad (5)$$

where $f = F/RT$, $E_{f,1}^0$ being the formal potential of the Ox_1/Red_1 couple, while P_1 and P_2 are the parameters controlling the slope and position of the main region of the negative resistance on the potential axis. The thermodynamic dependence (eq 5) between $k_{f,1}$ and $k_{b,1}$ means that the sum of the cathodic (αn) and anodic (βn) transfer coefficients equals to the number of electrons involved in the electrode process: $\alpha n + \beta n = n$, which is concordant with literature data.[19]

For the process in (3) the simple dependence of $k_{f,2}$ on E was assumed, since the detailed characteristics of the catalytic electroreduction of azides is not precisely known:

$$k_{f,2} = k_{s,2}^{app}\exp[-(\alpha n)_2 f(E-E_{f,2}^0)] \quad (6)$$

$$k_{b,2} = 0$$

(i.e., process 3 in anodic direction is not considered) (7)

where $E_{f,2}^0$ is the formal potential of the Ox_2/Red_2 couple.

The general analytical expression for the faradaic current, controlled by the charge-transfer step of the process studied at the streaming electrode, is known.[26] It comes from the expression for the instantaneous faradaic current,[40,41] applied to an elementary segment of a surface area $dA = 2\pi r\, dl$ of a streaming electrode:

$$dI_f = -nFc_{ox}^0 k_f \exp(\kappa^2 t)\,\mathrm{erfc}(\kappa t^{1/2})\,dA = 2\pi rnFc_{ox}^0 k_f \exp(\kappa^2 t)\,\mathrm{erfc}(\kappa t^{1/2})\,dl \quad (8)$$

integrated over the entire electrode length $l = [0, l_{max}]$ or the corresponding electrolysis time t varying from 0 to $t_{max} = l_{max}/v$. The expression for the steady-state faradaic current is then obtained:

$$I_{f,ss} = -2\pi rnFc_{ox}^0 k_f v\int_0^{t_{max}} \exp(\kappa^2 t)\,\mathrm{erfc}(\kappa t^{1/2})dt = -2\pi rnFc_{ox}^0 k_f v\left[\frac{2}{\kappa}\sqrt{\frac{t_{max}}{\pi}} + \frac{\exp(\kappa^2 t_{max})\,\mathrm{erfc}(\kappa {t_{max}}^{1/2}) - 1}{\kappa^2}\right] \quad (9)$$

In eqs 8 and 9, the minus sign is introduced for making the cathodic current negative, and the κ parameter, relating the kinetics of the charge transfer and diffusion transport, keeps its usual definition: $\kappa = (k_f/{D_{ox}}^{1/2}) + (k_b/{D_{red}}^{1/2})$.

According to the complex characteristics of the electrode processes considered here the total faradaic current corresponding to reaction scheme in eqs 2 and 3 is a sum of contributions from the corresponding parallel reaction pathways, i.e.:

$$I_{f,ss} = -2\pi rnFv\left\{c_{ox,1}^0 k_{f,1}\left[\frac{2}{\kappa_1}\sqrt{\frac{t_{max}}{\pi}} + \frac{\exp({\kappa_1}^2 t_{max})\,\mathrm{erfc}(\kappa_1 {t_{max}}^{1/2}) - 1}{{\kappa_1}^2}\right] + c_{ox,2}^0 k_{f,2}\left[\frac{2}{\kappa_2}\sqrt{\frac{t_{max}}{\pi}} + \frac{\exp({\kappa_2}^2 t_{max})\,\mathrm{erfc}(\kappa_2 {t_{max}}^{1/2}) - 1}{{\kappa_2}^2}\right]\right\} \quad (10)$$

where $n = n_1 = n_2 = 2$ and the kinetic parameters κ_1 and κ_2 are defined as

$$\kappa_1 = \frac{k_{f,1}}{{D_{ox,1}}^{1/2}} + \frac{k_{b,1}}{{D_{red,1}}^{1/2}};\ \kappa_2 = \frac{k_{f,2}}{{D_{ox,2}}^{1/2}} \quad (11)$$

TABLE 1: Fitted and Assumed Electrochemical Parameters for the Electroreduction of Azide Complexes of Nickel(II) Corresponding to Experimental *I*−*E* Characteristics and Conditions from Figure 1, Parts A and B

parameter	value for the *I*−*E* from Figure 1A	value for the *I*−*E* from Figure 1B	source
$k_{s,I}^{app}$	5.6×10^{-5} cm s^{-1}	4.5×10^{-5} cm s^{-1}	ref 19
$k_{s,II}^{app}$	2.0×10^{-10} cm s^{-1}	3.0×10^{-10} cm s^{-1}	this paper
$k_{s,2}^{app}$	3×10^{-2} cm s^{-1}	3×10^{-2} cm s^{-1}	this paper
P_1	-64 V^{-1}	-60.8 V^{-1}	this paper
P_2	-0.784 V	-0.802 V	this paper
$(\alpha n)_I$	1.47	1.47	ref 19 and this paper
$(\alpha n)_{II}$	0.52	0.52	ref 19 and this paper
$(\alpha n)_2$	0.50	0.50	this paper
$E_{f,1}^0$	-0.641 V	-0.666 V	this paper
$E_{f,2}^0$	-1.100 V	-1.100 V	this paper
E_{pzc}	-0.583 V	-0.605 V	this paper
$D_{ox,1}$	6.9×10^{-6} cm^2 s^{-1}	6.9×10^{-6} cm^2 s^{-1}	ref 19
$D_{red,1}$	6.5×10^{-6} cm^2 s^{-1}	6.5×10^{-6} cm^2 s^{-1}	ref 43
$D_{ox,2}$	6.5×10^{-6} cm^2 s^{-1}	6.5×10^{-6} cm^2 s^{-1}	this paper
K	25.7 μF cm^{-2}	27.0 μF cm^{-2}	this paper
c_{ox1}^0	2.0×10^{-3} mol dm^{-3}	4.0×10^{-3} mol dm^{-3}	this paper
c_{ox2}^0	4.8×10^{-4} mol dm^{-3}	6.0×10^{-4} mol dm^{-3}	this paper

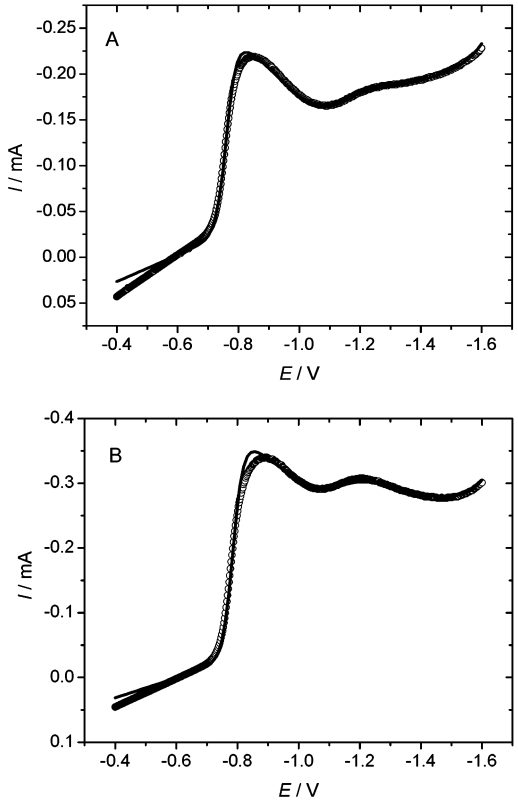

Figure 9. Results of fittings of the sum of the theoretical faradaic (eq 10) and capacitive (eq 12) currents (−) to the experimental points (○) of the *I*−*E* characteristics from (A) Figure 1A and (B) Figure 1B. For model parameters, see Table 1.

Typical of the streaming electrodes, there is also a permanent flow of the *steady-state capacitive* current $I_{c,ss}$

$$I_{c,ss} = K(E - E_{pzc})\frac{dA}{dt} = 2\pi rK(E - E_{pzc})\frac{d\,l}{d\,t} = 2\pi rK(E - E_{pzc})v \quad (12)$$

where $A = 2\pi rl$ is the side cylindrical surface of the electrode of a radius r, undergoing permanent renewal with the velocity $v = dl/dt$, E_{pzc} being the point of zero charge of mercury electrode in contact with a given solution, and $K = (1/(E - E_{pzc})) \times \int_{E_{pzc}}^{E} C_d\, dE$ is the *integral* double layer capacitance per unit area which better than the (generally potential-dependent) differential capacitance C_d at given E describes the charging of the fresh mercury surface from E_{pzc} to the imposed potential E.[23,42]

Equations 10 and 12 constitute the basis for the determination of unknown parameters of the studied electrode process. For that purpose the $I = (I_{f,ss} + I_{c,ss}) = f(E)$ functional dependence was fitted to the experimental data from Figure 1, part A or B, respectively. Some of the parameters, as e.g. $k_{s,I}^{app}$, $D_{Ox,1}$, $D_{Red,1}$, and E_{pzc} were not fitted but were taken from the literature[19,43] or determined in our present studies. For significant mathematical simplification of the later numerical determination of the multiple steady states, we used not the potential-dependent, but the constant integral capacitance, averaged over the potential range [−0.8, −1.5 V] within which the NDR regions develop. The results of such fittings are graphically presented in Figure 9, parts A and B, respectively, whereas all the fitted and assumed parameters are collected in Table 1.

4.3.2. Theoretical Determination of the Full Diagram of Steady States. The model electrochemical characteristics of the electroreduction of the azide complexes can now be used for the construction of the folded diagram of the stable and unstable steady states in the presence of a given serial resistance R_s in the circuit. The method of calculations described below is different from our earlier approach,[20] applied for the description of bistability in the electroreduction of Ni(II)−SCN^- complexes. Now, instead of building up a purely numerical ("digital simulation") model, based on the discretization of the spatial and time coordinates of the streaming electrode and the adjacent solution, we use the numerical method only for the search for the faradaic and capacitive currents as the roots of the combined analytical relationships for these currents (eqs 10 and 12). Calculations done with the present method are much easier and also require much less computation time. We used this approach already for the alternative calculation of the diagram of stable and unstable steady states for the Ni(II)−SCN^- electroreduction,[21] but without a detailed description of this algorithm which is given in this paper.

The principle of calculations is as follows. In the presence of serial resistance R_s the ohmic drops make the interfacial

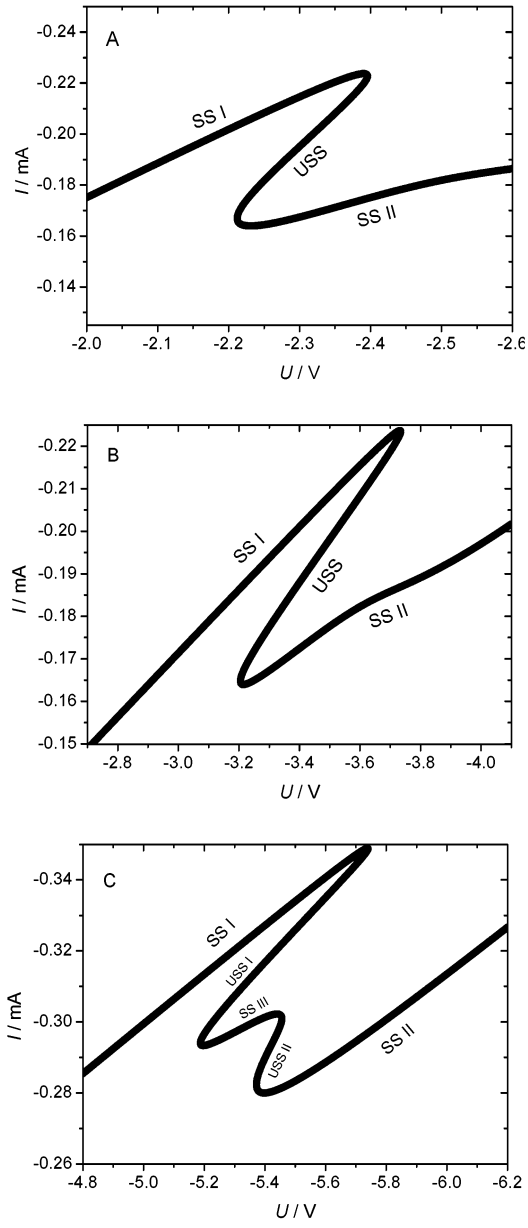

Figure 10. Theoretically calculated folded diagrams of stable and unstable multiple steady states for the model (eqs 2 and 3) electrochemical system: (A) bistability for the $I-E$ characteristics from Figure 9A, with $R_s = 7$ kΩ (cf. Figure 2); (B) as for part A, with $R_s = 13$ kΩ (cf. Figure 3); (C) bistable and tristable behavior for the $I-E$ characteristics from Figure 9B, with serial resistance $R_s = 14$ kΩ (cf. Figure 5).

potential drop E smaller than the externally applied voltage U

$$E = U - (I_{f,ss} + I_{c,ss})R_s \tag{13}$$

and this relation has to replace the simple electrode potential E in equations for the rate constants (eqs 4−6). The expression (eq 10) for the steady-state faradaic current becomes then implicit and contains also the capacitive current. The capacitive current can be further expressed as a function of the faradaic current through the combination of eqs 12 and 13:

$$I_{c,ss} = \frac{2\pi rK\nu(U - I_{f,ss}R_s - E_{pzc})}{1 + 2\pi rK\nu R_s} \tag{14}$$

This equation is replaced for the capacitive current in eq 10 with the electrode potential given by eq 13. Hence one obtains the final equation for the faradaic current I_f. Since this equation is implicit vs $I_{f,ss}$ as its root(s), the numerical method of searching for these solutions is applied. For a given voltage U, serial resistance R_s and other known parameters, the entire possible range of the faradaic current (i.e., the $[0, I_d]$ interval, with I_d defined by eq 1) is divided into the appropriate number of subintervals, and within each of them the roots are numerically searched for. We applied the particularly convenient and quickly convergent Müller's approach, which is the method of successive bisections and parabolic interpolation.[44] For the parameters' ranges corresponding to the multistable behavior we found in this way all steady-state solutions—both stable and unstable ones.

Results of such calculations, for the electrochemical characteristics of the systems collected in Table 1, are shown in Figure 10. These diagrams have the single-folded (for bistability) and double-folded (for tristability) shapes which should be compared with the experimental diagrams from Figures 2, 3, and 5, respectively. It is clear that the corresponding diagrams are very similar. Slight discrepancies observed are caused by the limited goodness of fit of the theoretical $I-E$ characteristics to the experimental ones; one should note that for the relatively high serial resistances R_s (here: 7−14 kΩ) even a relatively small uncertainty in the total current (e.g., 0.02 mA) results in a considerable (140−280 mV) shift of the corresponding (I,U) point on the U axis. Such a good concordance verifies both the principal mechanism of the origin of multistability in the electrode processes of Ni(II)−azide complexes and the validity of the proposed analytical-numerical approach for the theoretical determination of diagrams of multiple steady states. At the end of this analysis, it is useful to comment here the complete absence of spontaneous oscillations in the studied system, whereas for the previously [20] analyzed Ni(II)−SCN^- electroreduction oscillations were observed (but already in a very tiny parameter range, see Figures 4 and 5 in ref 20). The oscillatory instability is possible if the rate of the transport of the electroactive species toward the electrode surface is appropriately low in comparison to the charge-transfer rate, so that the surface concentration of this species can vary periodically as a function of time. It was still the case for the Ni(II)−SCN^- electroreduction, but the electroreduction rate of the Ni(II)−N_3 complexes never attains such high values (even the maximum current remains always below the diffusion-controlled value, as indicated above). Therefore, oscillations which were already close to the limit of detection for the Ni(II)−SCN^- electroreduction are not observed for the Ni(II)−N_3^- system, at least for a given set of $I-E$ characteristics.

4.4. Linear Stability Analysis of Steady States in the Ni(II)−N_3^- Electroreduction. The purely electrochemical characteristics of multistability in the Ni(II)−N_3 electroreduction can be now extended for the construction of the bifurcation diagrams based on the linear stability analysis in terms of the following dynamical variables: interfacial potential drop E and surface concentrations $c_{ox}(0,t)$ (further also abbreviated by c_s) of the Ox reactants. Two reactants (Ox_1 and Ox_2) are actually considered, so the system of three ordinary differential equations is necessary for the full description of dynamics of the Ni(II)−N_3^- electroreduction:

$$\frac{dE}{dt} = \frac{U-E}{2\pi r R_s K l_{max}} - \frac{(E-E_{pzc})v}{l_{max}} + \frac{nFk_{f,1}c_{ox,1}(0,t)}{K} + \frac{nFk_{f,2}c_{ox,2}(0,t)}{K} \equiv F[E,c_{ox,1}(0,t),c_{ox,2}(0,t)] \quad (15)$$

$$\frac{dc_{ox,1}(0,t)}{dt} = -\frac{2k_{f,1}c_{ox,1}(0,t)}{\delta_N} + \frac{2D_{ox,1}[c^0_{ox,1} - c_{ox,1}(0,t)]}{\delta_N{}^2} \equiv G[E,c_{ox,1}(0,t)] \quad (16)$$

$$\frac{dc_{ox,2}(0,t)}{dt} = -\frac{2k_{f,2}c_{ox,2}(0,t)}{\delta_N} + \frac{2D_{ox,2}[c^0_{ox,2} - c_{ox,2}(0,t)]}{\delta_N{}^2} \equiv H[E,c_{ox,2}(0,t)] \quad (17)$$

For the explanation of the form of these equations, including all the simplifications underlying their derivation, see ref 21. Two important simplifications will be reminded here. First, the anodic direction of process 2 is neglected (i.e., $k_{b,1} = 0$), as the apparent rate constant $k^{app}_{s,I}$ is not high and the region of a negative resistance appears at potential considerably more negative that the formal potential $E^0_{f,1}$. Second, eqs 15−17 correspond to the simplified model of the virtual streaming electrode of a constant (average) thickness of the diffusion layer $\bar{\delta}_N$, the choice of which affects the quantitative characteristics of the stability diagram. For our real streaming electrode the diffusion layer varies from 0 at the glass capillary orifice to ca. $\delta_N = (\pi D_{ox} t_{max})^{1/2} \approx 2\ \mu$m at the end of the mercury stream. For calculations presented below, we chose the reasonable medium value $\bar{\delta}_N = 1.05\ \mu$m, which ensured the possibly good concordance between the experimental and theoretical diagrams.

The Jacobian matrix of the characteristic equation, corresponding to the system of eqs 15−17 after linearization around the given steady state, has the form shown in eq 18, where according to analytical expressions 4 and 6 for the $k_{f,1}$ and $k_{f,2}$ rate constants, the

$$\mathbf{J} = \begin{bmatrix} \left(\frac{\partial F}{\partial E}\right)_{ss} & \left(\frac{\partial F}{\partial c_{s,1}}\right)_{ss} & \left(\frac{\partial F}{\partial c_{s,2}}\right)_{ss} \\ \left(\frac{\partial G}{\partial E}\right)_{ss} & \left(\frac{\partial G}{\partial c_{s,1}}\right)_{ss} & \left(\frac{\partial G}{\partial c_{s,2}}\right)_{ss} \\ \left(\frac{\partial H}{\partial E}\right)_{ss} & \left(\frac{\partial H}{\partial c_{s,1}}\right)_{ss} & \left(\frac{\partial H}{\partial c_{s,2}}\right)_{ss} \end{bmatrix} =$$

$$\begin{bmatrix} \frac{-1}{2\pi r R_s K l_{max}} - \frac{v}{l_{max}} + \frac{nFc_{ss,1}}{K}\left(\frac{dk_{f,1}}{dE}\right)_{ss} + \frac{nFc_{ss,2}}{K}\left(\frac{dk_{f,2}}{dE}\right)_{ss} & \frac{nFk_{f,1}(E_{ss})}{K} & \frac{nFk_{f,2}(E_{ss})}{K} \\ -\frac{2c_{ss,1}}{\bar{\delta}_N}\left(\frac{dk_{f,1}}{dE}\right)_{ss} & -\frac{2k_{f,1}(E_{ss})}{\bar{\delta}_N} - \frac{2D_{ox,1}}{\bar{\delta}_N{}^2} & 0 \\ -\frac{2c_{ss,2}}{\bar{\delta}_N}\left(\frac{dk_{f,2}}{dE}\right)_{ss} & 0 & -\frac{2k_{f,2}(E_{ss})}{\bar{\delta}_N} - \frac{2D_{ox,2}}{\bar{\delta}_N{}^2} \end{bmatrix} \quad (18)$$

derivatives $dk_{f,1}/dE$ and $dk_{f,2}/dE$ are given by the following relationships:

$$\left(\frac{dk_{f,1}}{dE}\right)_{ss} = \frac{-(\alpha n)_I f k^{app}_{s,I} \exp[-(\alpha n)_I f(E_{ss} - E^0_{f,1})]}{1 + \exp[P_1(E_{ss} - P_2)]} - \frac{P_1 \exp[P_1(E_{ss} - P_2)] k^{app}_{s,I} \exp[-(\alpha n)_I f(E_{ss} - E^0_{f,1})]}{\{1 + \exp[P_1(E_{ss} - P_2)]\}^2} -$$

$$(\alpha n)_{II} f k^{app}_{s,II} \exp[-(\alpha n)_{II} f(E_{ss} - E^0_{f,1})] \quad (19)$$

$$\left(\frac{dk_{f,2}}{dE}\right)_{ss} = -(\alpha n)_2 f k^{app}_{s,2} \exp[-(\alpha n)_2 f(E_{ss} - E^0_{f,2})] \quad (20)$$

In our calculation procedure, for a given voltage U and serial resistance R_s, first all the possible steady-state potentials E_{ss} were found numerically (using Müller's method) as the roots of the equation:

$$\frac{U - E_{ss}}{2\pi r R_s K l_{max}} - \frac{(E_{ss} - E_{pzc})v}{l_{max}} + \frac{nFk_{f,1}(E_{ss})c^0_{ox,1}D_{ox,1}}{K[D_{ox,1} + k_{f,1}(E_{ss})\bar{\delta}_N]} + \frac{nFk_{f,2}(E_{ss})c^0_{ox,2}D_{ox,2}}{K[D_{ox,2} + k_{f,2}(E_{ss})\bar{\delta}_N]} = 0 \quad (21)$$

that comes from the combination of eqs 15−17 with the simultaneously imposed steady-state (fixed point) condition $dE/dt = dc_{s,1}/dt = dc_{s,2}/dt = 0$. The corresponding steady-state surface concentrations $c_{ss,1}$ and $c_{ss,2}$ are then calculated from eqs 16 and 17 with $E = E_{ss}$ and $dc_{s,1}/dt = dc_{s,2}/dt = 0$. For these stationary states the values of the corresponding determinant Det and the trace Tr of the Jacobian matrix (eq 18) were calculated. Repeating of this procedure for the set of values of U and R_s allows one to determine the position of points corresponding to the saddle-node (Det(**J**) = 0) and Hopf bifurcations (Tr(**J**) = 0 with Det(**J**)>0). The stability diagrams constructed from these conditions, for the system's parameter corresponding to $I-E$ characteristics from Figure 9, parts A and B, are shown in Figure 11, parts A and B, respectively. Their comparison with Figures 4 and 6 exhibits distinct similarities what proves the validity of this way of analysis.

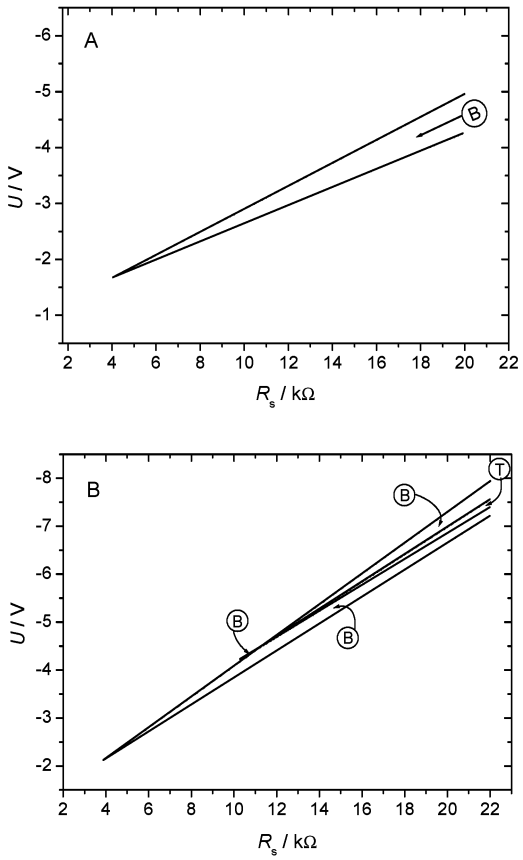

Figure 11. Theoretical bifurcation diagrams corresponding to the *I*−*E* characteristics from (A) Figure 9A, showing the regions of bistability, and (B) Figure 9B, showing the regions of bi- and tristability, denoted with letters B and T, respectively. In both diagrams the lines separating different regions correspond to the saddle-node bifurcations (Det(**J**) = 0). The Hopf bifurcations (Tr(**J**) = 0 with Det(**J**)>0) were not detected which confirms the experimentally observed lack of oscillations.

One should also note one more important conclusion—according to our experimental results, the present theoretical stability diagrams (contrary to that for the Ni(II)−SCN^- electroreduction[21]) do not contain any points corresponding to the Hopf bifurcation, so the oscillations in the studied process are indeed impossible. The bifurcation diagrams from Figure 11 constitute thus the independent proof that the complete lack of oscillations in the experimental investigations of the Ni(II)−N_3^- electroreduction at a streaming mercury electrode, *at least characterized by the I*−*E dependencies from Figure 1*, was a true result, fully justified by the dynamics of this process.

In principle, the system of three ordinary differential equations could generate also more complex dynamic behaviors than the ones described here but since they were not observed in our experiments, we limited the theoretical analysis to the realistic parameters ranges and to the explanation of really observed phenomena. Therefore, the analysis presented in this paper, made in terms of both electrochemical properties of the system and standard techniques of nonlinear dynamics, completes the description of a new multistable electrochemical system, based on the electroreduction of Ni(II)−N_3^- complexes at a streaming mercury electrode.

5. Summary and Conclusions

We described the new electrochemical bistable/tristable system that combines the properties of the streaming mercury electrode with the complex electrochemical mechanism of the electroreduction of the azide complexes of nickel(II). This process is associated with the formation of the negative differential resistance in its *I*−*E* characteristics that is the main source of instabilities of steady states for appropriate experimental conditions. Furthermore, since not only the central ion, but also the ligand can undergo electroreduction (with the participation of H^+ ions), the *I*−*E* characteristics can be deformed with the formation of two sequential regions of NDR. Then not only bistability but also tristability can be observed on the *I*-*U* curves when external voltage *U* is scanned toward negative and positive values. We constructed the experimental diagrams of stable and unstable steady states for given conditions. The systematic studies of the possible dynamic behaviors led us to the construction of the experimental bifurcation diagrams in the *U*-R_s parameter space that showed the areas of mono- and multistability (separated by points of the saddle-node bifurcations). The sustained oscillations were not observed since the rate of transport of the Ni(II)−N_3^- complexes toward the electrode surface is too fast compared to the rate of the charge-transfer step, and therefore, the surface concentration of the reactant cannot undergo periodical changes around the given steady state.

Using the analytical expressions for the faradaic and capacitive currents we determined the thermodynamic and kinetic parameters of the studied redox system by comparison of the experimental and theoretical *I*−*E* dependencies. We used these relationships for the numerical determination of diagrams of stable and unstable steady states that explain the bistable or tristable behavior of the system, in the presence of appropriate serial resistance in the electric circuit. Finally, in terms of the linear stability analysis, we constructed the theoretical bifurcation diagrams that are well concordant with the analogous experimental diagrams. In particular, the lack of oscillations for the studied experimental conditions was also confirmed by these theoretical diagrams.

The electroreduction of Ni(II)−N_3^- process studied at the streaming mercury electrode is one of only a few examples of tristability found for real chemical systems.

References and Notes

(1) Glansdorff, P.; Prigogine, I. *Thermodynamic theory of structure, stability and fluctuations*; Wiley-Interscience: London, 1971.
(2) Nicolis, G.; Prigogine, I. *Self-organization in Nonequilibrium Systems*; Wiley: New York, 1977.
(3) Gray, P.; Scott, S. K. *Chemical Oscillations and Instabilities*; Clarendon Press: Oxford, England, 1990.
(4) Field, R. J.; Györgyi, L. *Chaos in Chemistry and Biochemistry*; World Scientific: Singapore, 1993.
(5) Field, R. J.; Burger, M. Eds.; *Oscillations and Travelling Waves in Chemical Systems*; Wiley-Interscience: New York, 1985.
(6) Bergé, P.; Pomeau, Y.; Vidal, C. *Order Within Chaos. Towards a Deterministic Approach to Turbulence*; Wiley-Herman: Paris, 1984.
(7) Orlik, M. *Oscillating reactions*−*Order and Chaos*; WNT: Warsaw, 1996 (in Polish).
(8) Strogatz, S. H. *Nonlinear Dynamics and Chaos*; Addison-Wesley: Reading, MA, 1994.
(9) Krischer, K. In *Modern Aspects of Electrochemistry 32*; Bockris, J. O.'M., Conway, B. E., White, R. E., Eds.; Kluwer/Academic/Plenum Press: New York, 1999; p 1.
(10) Orbán, M.; Dateo, C.; De Kepper, P.; Epstein, I. R. *J. Am. Chem. Soc.* **1982**, *104*, 5911.
(11) Alamgir, M.; Epstein, I. R. *J. Am. Chem. Soc.* **1983**, *10*, 2500.
(12) Nagy, A.; Treindl, L. *J. Phys. Chem.* **1989**, *93*, 2807.
(13) Chie, K.; Okazaki, N.; Tanimoto, Y.; Hanazaki, I. *Chem. Phys. Lett.* **2001**, *334*, 55.
(14) Tockstein, A. *Chem. Phys. Lett.* **1992**, *188*, 5.
(15) Ganapathisubramanian, N. *J. Phys. Chem.* **1992**, *96*, 4446.
(16) Schell, M. *J. Electroanal. Chem.* **1998**, *457*, 221.
(17) Chen, S.; Schell, M. *J. Electroanal. Chem.* **1999**, *478*, 108.
(18) Chen, S.; Schell, M. *Electrochim. Acta* **2000**, *45*, 3069.
(19) Kutner, W.; Galus, Z. *J. Electroanal. Chem.* **1974**, *51*, 363.

(20) Jurczakowski, R.; Orlik, M. *J. Phys. Chem. B* **2002**, *106*, 1058.
(21) Orlik, M.; Jurczakowski, R. *J. Phys. Chem. B* **2002**, *106*, 7527.
(22) *Complexometric Assay Methods with Titriplex*, 3rd ed.; E. Merck: Darmstadt, Germany, 1982.
(23) Galus, Z., Ed. *Electroanalytical Methods of Determination of Physicochemical Constants*; PWN: Warsaw, 1979 (in Polish).
(24) Kotrlý, S.; Šůcha, L. *Handbook of Chemical Equilibria in Analytical Chemistry*; SNTL/Ellis Horwood/Wiley: Chichester, England, 1985.
(25) Weaver, R. J.; Parry, R. W. *J. Am. Chem. Soc.* **1954**, *76*, 6258.
(26) Weaver, R. J.; Parry, R. W. *J. Am. Chem. Soc.* **1956**, *78*, 5542.
(27) Jurczakowski, R.; Orlik, M. Manuscript in preparation.
(28) Maggio, F.; Romano, V.; Pellerito, L. *J. Electroanal. Chem.* **1967**, *15*, 227.
(29) Senise, P.; Godinho, O. E. S. *J. Inorg. Nucl. Chem.* **1970**, *32*, 3641.
(30) Tamamushi, R.; Matsuda, K. *J. Electroanal. Chem.* **1966**, *12*, 436.
(31) Koper, M. T. M.; Sluyters, J. H. *J. Electroanal. Chem.* **1993**, *352*, 51.
(32) Jurczakowski, R.; Orlik, M. *J. Electroanal. Chem.* **1999**, *478*, 118.
(33) Jurczakowski, R.; Orlik, M. *J. Electroanal. Chem.* **2000**, *486*, 65.
(34) de Levie, R. *J. Electrochem. Soc.* **1971**, *118*, 185C.
(35) de Levie, R. *J. Electroanal. Chem.* **1970**, *25*, 257.
(36) Pospišil, L.; de Levie, R. *J. Electroanal. Chem.* **1970**, *25*, 245.
(37) Koper, M. T. M.; Sluyters, J. H. *J. Electroanal. Chem.* **1991**, *303*, 65.
(38) Koryta, J. *Collect. Czech. Chem. Commun.* **1954**, *19*, 433.
(39) Śledziewski, R. *Electronics for the Physics Students*; PWN: Warsaw, 1978 (in Polish).
(40) Delahay, P. *J. Am. Chem. Soc.* **1953**, *75*, 1430.
(41) Galus, Z. *Fundamentals of Electrochemical Analysis*, 2nd ed., Ellis Horwood/PWN: Warsaw, 1994.
(42) Delahay, P. *J. Electroanal. Chem.* **1965**, *10*, 1.
(43) Gumiński, C. *J. Mater. Sci.* **1989**, *24*, 2661.
(44) Kristiansen, G. K. *BIT* **1963**, *3*, 205.